Circular Dichroism and Magnetic Circular Dichroism Studies of the Biferrous Form of the R2 Subunit of Ribonucleotide Reductase from Mouse: Comparison to the R2 from *Escherichia coli* and Other Binuclear Ferrous Enzymes†

Kari R. Strand,‡ Yi-Shan Yang,§,|| K. Kristoffer Andersson,*,‡ and Edward I. Solomon*,§

Department of Biochemistry, University of Oslo, NO-0316 Oslo, Norway, and Department of Chemistry, Stanford University, Stanford, California 94305

Received July 16, 2003; Revised Manuscript Received August 28, 2003

ABSTRACT: Ribonucleotide reductase (RNR) catalyzes the synthesis of the four deoxyribonucleotides needed for DNA synthesis and repair in living organisms. The reduced [Fe(II)Fe(II)] form of the model mammalian enzyme, mouse RNR R2, has been studied using a combination of circular dichroism (CD), magnetic circular dichroism (MCD), and variable-temperature variable-field (VTVH) MCD spectroscopies. Titrations of ferrous ion to the apo-enzyme have been performed and analyzed to investigate the metal binding affinity of the metal-binding site. Spectral features of individual iron sites have been analyzed to obtain detailed geometric and electronic structural information. VTVH MCD data have been collected and analyzed using two complementary models to obtain detailed ground state information including the zero-field splitting (ZFS) of both ferrous centers and the exchange coupling (*J*) between the two sites. These ground and excited state results provide a complete description of the biferrous site of mouse R2. The biferrous site consists of one 4- and one 5-coordinate iron, with positive and negative ZFS values, respectively. Weak exchange coupling between the two ferrous centers is present, consistent with having carboxylate bridges. The two sites have highly cooperative and weak metal binding affinities. This may be a novel regulatory mechanism for RNR. These results are compared with those from reduced *Escherichia coli* R2 and reduced acyl-carrier protein Δ^9 desaturase to correlate to similarities and differences in their dioxygen reactivity.

Binuclear iron−oxygen active sites have been found in a number of metalloproteins performing a variety of biological functions (*1*−*4*). Their binuclear centers show magnetic coupling associated with bridging ligands and can exist in different oxidation states. The most common states are the oxidized [Fe(III)Fe(III)], the mixed-valent [Fe(III)Fe(II)], and the reduced [Fe(II)Fe(II)] states (*3*−*12*). Some of the members of this class are the hydroxylase component of methane monooxygenase (MMOH), the acyl-carrier protein Δ^9 desaturase (Δ^9D)[1], and the R2-dimer of ribonucleotide reductase (RNR). They share similarities in their overall 3-D structures and the physical properties of their binuclear iron−oxygen sites. They all activate dioxygen to form intermediates including $[Fe(III)]_2$-peroxo and a high-valent Fe(IV)-oxo species (*13*−*23*). The fully reduced state [Fe(II)Fe(II)] is of particular interest from a biochemical standpoint as it is the state that reacts with dioxygen in these enzymes. RNR reacts with dioxygen to generate an essential tyrosine radical needed for the synthesis of deoxyribonucleotides. MMOH hydroxylates methane to methanol; an activating/coupling protein (component B, MMOB) is required for the rapid reaction with dioxygen (*24*, *25*). Δ^9D catalyzes the insertion of a cis double bond in fatty acid biosynthesis to convert stearoyl-ACP to oleoyl-ACP; substrate (stearoyl-acyl carrier protein) must be bound to the enzyme for the dioxygen reaction (*26*). Resting reduced R2 RNR is the only enzyme among the three that reacts rapidly with dioxygen without the prior formation of slow protein−protein or protein−substrate complexes, as the substrate, a tyrosine residue, is already present at the iron site. The functional diversity of this group of enzymes (desaturation, hydroxylation, and radical formation) is reflected in the oxidation of the diferrous enzymes. It is thus of importance to understand how the electronic and structural differences of these reactive reduced sites contribute to this diverse range of reactivities.

† Financial support was provided by the Norwegian Research Council, the Norwegian Cancer Society, and the EU TMR Program ERBMRFXCT980207 (K.K.A.) (Iron−Oxygen Protein network), the Norwegian Research Council travel grants (K.R.S.), and the NSF−Biophysics Program Grant MCB 9816051 (E.I.S.).

* To whom correspondence should be addressed. (E.I.S.) Phone: (650) 723-9104. E-mail: edward.solomon@stanford.edu. (K.K.A.) Phone: +47 2285-6625. E-mail: k.k.andersson@biokjemi.uio.no.

‡ University of Oslo.

§ Stanford University.

|| Current address: Lucas Magnetic Resonance Spectroscopy and Imaging Center, Department of Radiology, Stanford University Medical School, Stanford, CA 94305.

[1] Abbreviations: ACP, acyl-carrier protein; Δ^9D, acyl-carrier protein Δ9-desaturase; CD, circular dichroism; MCD, magnetic circular dichroism; MMO, iron form of methane monooxygenase; MMOB, B component of the iron form of methane monooxygenase; MMOH, hydroxylase component of the iron form of methane monooxygenase; RNR, ribonucleotide reductase; RNR R2, R2 subunit of ribonucleotide reductase; SQUID, superconducting quantum interferometer device; VTVH MCD, variable-temperature variable-field magnetic circular dichroism; ZFS, zero-field splitting.

10.1021/bi035248q CCC: $25.00
Published on Web 10/04/2003

The synthesis of the four deoxyribonucleotides catalyzed by RNR is a unique pathway for DNA synthesis and repair in all living organisms (*27*, *28*). So far, three classes of RNR have been characterized based on their sequences and cofactors (*29*−*32*). Class I RNR, which is the focus of this study, is found in all eukaryotes and in some microorganisms such as *Escherichia coli*. This class of enzymes is a complex of two dimeric proteins called R1 and R2. A binuclear iron−oxygen center and a stable tyrosyl radical that is essential for enzymatic activity are located in each monomer of R2. The R1-dimer contains the substrate binding site with the postulated catalytic essential thiyl radical. This thiyl-radical in R1 is formed by being transferred from the R2 tyrosyl radical via an array of hydrogen bonded amino acids (*31*, *33*, *34*). Class I RNR is further divided into two subclasses, class Ia and Ib, according to their sequences, structure of the tyrosyl radicals, and allosteric regulation and reductants used in vivo. Class Ia is present in both prokaryotes and eukaryotes, class Ib is found only in prokaryotes, and some bacteria code for both subclasses. Their tyrosyl radicals have different dihedral angles between the tyrosyl plane and the β-protons, and some tyrosyl radicals can be hydrogen bonded (*35*).

RNR isolated from both mouse and *E. coli* belongs to class Ia RNR. The mouse RNR is the first mammalian enzyme isolated in the RNR family. The *E. coli* RNR is by far the best-characterized enzyme and the prototype of class Ia RNRs. Although the amino acids that coordinate the metal ions, the tyrosyl radical, and the amino acid in the proposed radical transport chain from R2 to R1 are conserved for the mouse and the *E. coli* R2, several significant differences among the two enzymes are observed. The overall amino acid sequence identity between the *E. coli* R2 and the mouse R2 is only about 25% (*36*), while there is high sequence identity among the eukaryotic R2 proteins distributed over the whole sequence (60−82%) (*37*). Thus, mouse R2 can be considered as a better model for the eukaryotic RNRs of class Ia. The iron center is more labile in mouse R2 (*38*, *39*), and the diiron/radical cluster showed significantly different redox properties from *E. coli* R2. The reduced mouse R2 exhibits an integer EPR signal in perpendicular or parallel mode with an observed *g* value around 14 in 20% glycerol (*40*) that is not observed for the *E. coli* enzyme. The exchange coupling between the irons in the active oxidized state is weaker in mouse than in *E. coli*. The mixed-valence form [Fe(II)Fe(III)] of mouse R2 can be induced by mild chemical reduction to a yield of 30% (*40*, *41*). In the *E. coli* R2 protein, this redox state is only produced to limited quantity (yield ∼5%) using drastic conditions.

In the X-ray structure of the reduced binuclear *E. coli* R2 center, both ferrous ions are 4-coordinate and bridged by two carboxylate ligands Glu 238 and Glu 115 in a μ-1,3 configuration (*8*). The two ferrous ions are separated by 3.9 Å. The ligands coordinated to Fe1 are His 241 and monodentate Glu 204. His 118 and monodentate Asp 84 are bound to Fe2 (the iron closest to the tyrosyl radical). Alternatively, a combination of circular dichroism (CD)/magnetic circular dichroism (MCD)/variable-temperature variable-field (VTVH) MCD in the near-IR region have shown that the reduced binuclear site of R2 in solution exhibits spectral features corresponding to one 5-coordinate and one 4-coordinate iron site. The two ferrous atoms are weakly antiferromagnetically coupled, J equals approximately -0.5 cm^{-1}, and have opposite zero-field splitting (ZFS) values consistent with iron atoms in different coordination environments with the μ-1,3 carboxylate bridges (Scheme 1) (*42*).

Scheme 1

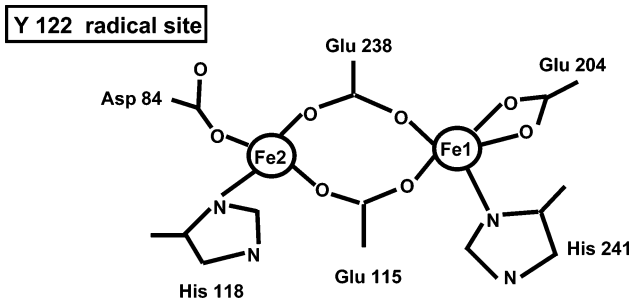

The first reported crystal structure of the mouse R2 protein was performed at pH 4.7, and the metal ion related electron density was observed only in the position equivalent to the iron site farthest away from the tyrosyl radical, Y177 (*37*). Recently, a structure of a fully occupied binuclear metal site was obtained for a cobalt substituted mouse R2 protein at a more physiological relevant pH (pH ∼6.0) (*43*). This structure reveals a high degree of flexibility in all the carboxylate ligands as compared to the structures for *E. coli* R2 and the mononuclear mouse R2. At present, the ligand environment of the site of the Fe(II)Fe(II) mouse R2 subunit of RNR is not known.

The geometric and electronic structures of the binuclear Fe(II) sites are difficult to probe. These active sites are not easily accessible through the traditional techniques such as X-band EPR. The d → d ligand field transitions are parity forbidden and thus weak in absorption in the near-IR spectral region (5000−16 000 cm^{-1}), which is obscured in absorption due to contributions from buffer and protein vibrations. However, CD measures the differential in absorption from the left and right circular polarized light, and these biferrous active sites exhibit signals in CD because they are chiral. In addition, since high-spin Fe(II) is paramagnetic with an $S = 2$ ground state, these active sites exhibit C-term MCD intensity that increases as temperature decreases and is orders of magnitude higher than the diamagnetic background in the liquid helium temperature (4.2 K) spectra. Thus, CD and MCD spectroscopies allow the observation of transitions to ligand field excited states that are weak in absorption, and the geometric and electronic structures of these binuclear Fe(II) sites can be elucidated using a combination of CD, low-temperature MCD, and variable-temperature variable-field (VTVH) MCD spectroscopies in the near-IR region (*2*).

The high-spin d^6 ferrous ion in an octahedral (O_h) ligand field has an orbitally triply degenerate $^5T_{2g}$ ground state and a doubly degenerate ^5E_g excited state split by $10Dq_{Oh}$. For biologically relevant nitrogen and oxygen ligation, $10Dq_{Oh}$ is approximately 10 000 cm^{-1}. The $^5T_{2g}$ and ^5E_g states are both split in energy due to the coordination environment of the reduced active site (*44*, *45*). Distorted 6-coordinate iron centers energetically split the ^5E state to produce a pair of transitions at around 10 000 cm^{-1} separated by up to ∼2000 cm^{-1}. Removal of an axial ligand leads to a 5-coordinate square-pyramidal (SP) geometry that shows two transitions, one around 5000 cm^{-1} and one at >10 000 cm^{-1}. Rearrangement of the five ligands toward a trigonal bipyramidal

(TBP) geometry decreases the transition energies, resulting in ligand field transitions at <5000 and <10 000 cm^{-1}. A 4-coordinate distorted tetrahedral ferrous site has $10Dq_{Td}$ equal to $-(4/9)10Dq_{Oh}$; thus, the highest energy ligand field transitions are in the 5000−7000 cm^{-1} region.

The VTVH MCD behavior of a ligand field transition can be further analyzed to estimate the ground state parameters of a coupled binuclear active site, including the total spin state and *g* values of the dimer ground and excited sublevels and the energies of the excited sublevels. These results can be further interpreted through a spin-Hamilitonian analysis to obtain the axial and rhombic zero-field splitting (ZFS) parameters *D* and *E* of each iron, which derive from the splitting of the single site $^5T_{2g}$ state, and the exchange coupling interaction (*J*) between the irons, which reflects the bridging ligands.

In this study, the reduced [Fe(II)Fe(II)] active site of mouse R2 is investigated using the CD/MCD/VTVH MCD methodology as described previously. The combination of the excited and ground state analysis provides detailed information about the geometric and electronic structure, as well as the interaction between the two irons in the active site of mouse R2. These results are significant as there are only limited data available for reduced mouse R2. We further compare these data to our prior results on reduced *E. coli* RR and reduced substrate-bound Δ^9 desaturase to define geometric and electronic structural similarities and differences and how these relate to dioxygen reactivity.

EXPERIMENTAL PROCEDURES

All commercial reagents were used as obtained: HEPES buffer (Sigma), potassium chloride (Sigma), ferrous ammonium sulfate hexahydrate (Mallinckrodt), deuterium oxide (99.9 atom % D, Aldrich), and d_3-glycerol (98 atom %, Cambridge Isotope Laboratories). The following procedures were conducted prior to use in an inert atmosphere: deuterated buffer was degassed by purging with 99.9% pure argon for at least 1 h; d_3-glycerol was degassed with at least 10 freeze−pump−thaw cycles at 10^{-3} Torr; protein samples were degassed by rapidly purging with at least 20 vacuum/argon cycles; and solid ferrous ammonium sulfate was pumped at 10^{-3} kPa for at least 1 h.

Mouse R2 protein was prepared as reported (*38*). The RNR R2 protein as obtained after purification was pretreated with 10 mM hydroxyurea and 5 mM EDTA at 4 °C for 20 min and passed down a 10 mL Sephadex G25 gel filtration column to remove all the iron and to reduce the tyrosyl radical before reconstitution with Fe(II). Deuterated buffer (50 mM Hepes, 100 mM KCl, pD 7.9) was added, and the solution was concentrated to ∼1.5−2 mM protein. This process was repeated until the percentage of D_2O was greater than 99.9% of the solvent and the protein concentration was in the range of 1.5−2 mM. The protein concentration was determined by using the molar extinction coefficient $\epsilon_{280-310}$ = 124 mM^{-1} cm^{-1}/ R2-dimer or a Bio-Rad protein assay (Bradford) (*46*).

The ferrous solution was obtained by anaerobically dissolving ferrous ammonium sulfate in degassed deuterated buffer to a final concentration of 50 mM. The appropriate amount of the ferrous ion solution was added anaerobically to the apoprotein and incubated for at least 10 min. The sample was transferred to an anaerobic cuvette for CD measurements. UV/vis and near-IR CD spectra showed no significant change with the addition of glycerol indicating no large conformational change due to glycerol. Protein samples (between 1.5 and 2.0 mM) were prepared for MCD studies by mixing with 50−60% (v/v) glycerol-d_3 pD 7.9. The sample was then immediately frozen in liquid nitrogen.

Circular dichroism studies were preformed on a JASCO J200D spectropolarimeter operating with a liquid nitrogen-cooled InSb detector in the 600−2000 nm region. Low-temperature magnetic circular dichroism data were acquired on this spectropolarimeter, modified to accommodate an Oxford Instrument SM4000-7T superconducting magnet capable of magnetic fields up to 7.0 T and temperatures down to 1.6 K.

Protein samples prepared for MCD studies were slowly inserted into the cryostat to reduce strain in the resulting optical glass. The depolarization of the protein glass was checked by measuring the CD spectrum of a freshly prepared nickel (+)-tartrate solution placed immediately before and after the MCD sample. Typically less than ∼5% of depolarization was observed.

The baseline-corrected CD and MCD spectra were fit to Gaussian band shapes using a constrained nonlinear least-squares fitting procedure. This determines the minimum number of ligand field transitions required to simultaneously fit the spectra. The transition energies and amplitude obtained are used for elucidating the geometric and electronic structures of the binuclear Fe(II) active sites and for estimating the binding constant of ferrous ion to apo-R2. Each spectroscopic method has a different selection rule; thus, transitions can have different amplitudes and signs, but the energies are similar. The MCD spectra are taken at low temperature (C-term MCD intensity is inversely proportional to temperature); thus, they may have significantly sharper bandwidths, and the band energies may shift a limited amount relative to the CD data. The CD spectra are taken at room temperature due to baseline effects in glycerol at low temperature, which are not present in MCD since the CD signal serves as the baseline. The amplitude, bandwidth, and energies of the CD and MCD transitions were allowed to float in the final fit. VTVH MCD data (MCD intensity, temperature, and applied magnetic field) were fit using a simplex routine that minimizes the χ^2 value. A goodness of fit parameter (χ^2/number of float parameters) was utilized to compare different fitting results.

RESULTS AND ANALYSIS

(1) Spectroscopy. (A) Fe(II) Binding Titration. (a) NIR CD. A titration of Fe(II) to mouse apo-R2 was followed by CD and MCD to elucidate the binding mode of Fe(II). Figure 1A shows the room-temperature CD titration of the apo form of mouse R2 with ferrous ion in the NIR region from 5500 to 13 000 cm^{-1}. In the presence of <2-fold equiv of ferrous ion, no CD signal is observed. The CD spectrum obtained with 2-fold Fe(II) loaded shows a very broad weak positive transition at about ∼7000 cm^{-1} and a weak negative transition at about 9700 cm^{-1}. The addition of 3 equiv of Fe(II) increases the intensity of both transitions by about 2-fold. The positions of the bands remain the same as more Fe was loaded into the protein. When 6 equiv of Fe(II) was

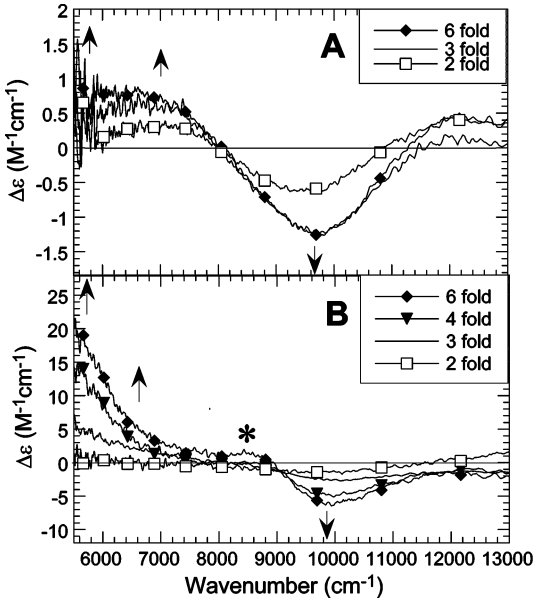

FIGURE 1: (A) CD spectra, recorded at 5 °C, of mouse RNR R2 in the presence of 2 (□), 3 (—), and 6 (◆) molar equivalents of ferrous ion. (B) MCD spectra, recorded at 5 K and 7 T, of mouse RNR R2 in the presence of 2 (□), 3 (—), 4 (▼), and 6 (◆) molar equivalents of ferrous ion. The peak in MCD marked with * is associated with the aqueous ferrous complex present in excess.

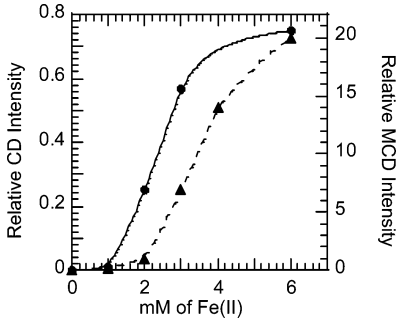

FIGURE 2: Formation of the binuclear Fe(II) cluster followed by the MCD transition at 5500 cm^{-1} and the CD transition at 7000 cm^{-1}. The dashed line presents the fit of the Hill equation to the MCD C-term intensity at 5500 cm^{-1} when different amounts of Fe(II) are added to apo-R2 ([R2] = 0.8 mM) (using the program GraFit Version 4 and nonlinear regression, Erithacus Software Limited, www.erithacus.com/grafit). The Hill coefficient from the fit is estimated to be 4.3 ± 0.1. The protein is half saturated when 3.6 mM Fe(II) is added to apoR2 ([R2-dimer] = 1.6 mM). The solid line presents the fit of the Hill equation to the CD absorption at 7000 cm^{-1} when different amounts of Fe(II) are added to apo-R2 ([R2] = 1.5 mM). The Hill coefficient from the fitting is estimated to be 4.9 ± 0.2. The protein is half saturated when 2.3 mM Fe(II) is added to apoR2 ([R2-dimer] = 3 mM).

added to the apoR2 form, the 9700 cm^{-1} band was saturated in intensity, while the intensity of the broad positive band at ~7000 cm^{-1} slightly increased.

(b) NIR MCD. Low-temperature MCD spectra were obtained for the samples corresponding to the room-temperature CD titration of apoR2 with Fe(II) (Figure 1B). The MCD spectrum upon the addition of 2 equiv of ferrous ion to the apo form shows one broad negative band at about 10 000 cm^{-1}. Two additional bands appear in the low-energy region at ~5500 and at ~6500 cm^{-1} (shoulder) when the ferrous ion concentration is >3.0-fold equiv.[2] At this concentration, the transition at about 10 000 cm^{-1} shows a 2-fold increase in intensity. The intensities of these transitions are not saturated with up to 6-fold ferrous added (Figures 1B and 2). Further addition of ferrous ion leads to precipitation of the protein.

(c) Cooperative Binding Model. For Fe(II) binding to apo-R2, the intensity of the MCD band at ~5500 cm^{-1} (Figure 2, dashed line) and the CD band at ~7000 cm^{-1} of one iron site (Figure 2, solid line) can be fit to a cooperative binding model using a Hill equation

$$Y = [L]^n/(K^n + [L]^n) \quad (1)$$

where $K = [P][L]^n/[PL_n]$ (P = protein, L = ligand = Fe(II), and n = Hill coefficient) and Y = fractional saturation = (MCD or CD intensity)/(saturated intensity). A Hill coefficient over 4 is obtained using nonlinear regression (4.3 for the MCD data and 4.9 for the CD data). This indicates that a strong cooperative interaction is present between the protein and the two binuclear Fe(II) centers. This is consistent with the highly cooperative binding of Co(II) to mouse apo-R2 (*43*) showing a Hill coefficient between 4 and 4.7. The affinity for the binuclear Fe(II) cluster for mouse R2 is low, as the mean of MCD and CD titrations is 2.8 mM for half-saturation (two of the four binding sites) of the R2-dimer (when concentration is normalized to [R2-dimer] = 1.6 mM).

(B) Gaussian Resolution and Peak Assignment. These CD and MCD titrations show that the affinity for Fe(II) is low and more than 4 equiv of Fe(II) are needed to saturate the four well-defined metal binding sites of the R2-dimer. The low affinity for Fe(II) in R2 indicates that there will be a significant amount of unbound ferrous ion in solution. This 6-coordinate hexaaqua-ferrous complex shows two weak positive MCD transitions at 9250 and 10 500 cm^{-1} (data not shown) but is not observed in the CD spectrum as it is not chiral. The MCD spectrum of the hexaaqua-ferrous complex is partially obscured by the negative MCD feature at 10 000 cm^{-1} associated with the active site iron, which shifts the effective peak maximum of the 9250 cm^{-1} band of aqueous Fe(II) to 8800 cm^{-1} in the MCD spectrum (Figure 1B). After subtraction of an amount of free iron in solution estimated from the binding constant from the observed MCD signal in the presence of 6 equiv of Fe(II), the peak in the 8800 cm^{-1} region significantly decreases, and the intensity of the negative peak at 10 000 cm^{-1} increases (compare Figures 1B and 3B).

The dashed lines in Figure 3A give the Gaussian resolution of the CD spectrum of the biferrous site. Three transitions are needed to fit the reduced R2 mouse CD spectra: two low-energy bands (5600 and 6700 cm^{-1}) and one high-energy band (9600 cm^{-1}). Figure 3B presents the Gaussian resolution of the MCD signals. Three peaks at 5500, 6800, and 10 000 cm^{-1} are also observed in the MCD spectrum. The presence of three transitions from both CD and MCD spectra in the NIR region indicate that the two Fe(II) atoms in the metal binding site have different coordination environments since a single Fe(II) ion cannot have more than two ligand field transitions above 5000 cm^{-1} (see introductory paragraphs). The presence of only one transition at an energy >8000 cm^{-1} indicates that neither iron is 6-coordinate, but one of the irons is 5-coordinate with a trigonal bipyramidal geometry. This

[2] It should be emphasized that while the ~5500 cm^{-1} band peaks near the cutoff of the NIR CD instrument, it is clearly present, and a band at this low energy has important structural implications.

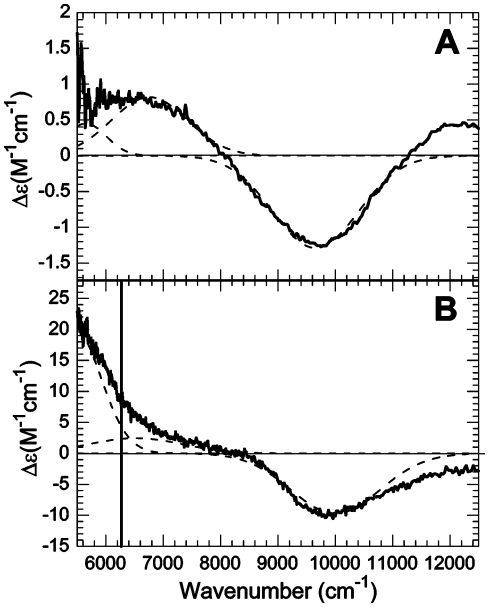

FIGURE 3: (A) CD and (B) LT MCD spectra of the binuclear non-heme Fe(II)Fe(II) active site mouse RNR R2. The experimental data (—) are fit to individual Gaussian band shapes (- - -). The CD and low-temperature MCD spectra were recorded at 5 °C and 5 K and 7 T, respectively. The vertical line in MCD marks the energy where the VTVH MCD data were collected (6250 cm^{-1}).

geometry should also have a second transition at <5000 cm^{-1}, which is below the range of our NIR instrument. The other two transitions at 5500 and 6800 cm^{-1} observed in both CD and MCD are correlated with the second iron (Fe2), and the energies of these transitions indicate the Fe2 is 4-coordinate with a distorted tetrahedral structure.

(2) Variable-Temperature Variable-Field (VTVH) MCD: Ground State Analysis. The MCD intensity of the reduced R2 increases as the temperature decreases, indicating that these transitions are MCD C-terms associated with paramagnetic doublets that are split by a magnetic field. Figure 4A,B shows the VTVH MCD saturation−magnetization curves of reduced R2 measured at 6250 cm^{-1} (symbols) utilizing two fitting results (line, vide infra). These VTVH MCD data were collected at the shoulder of the band associated with the 4-coordinate site. This band is the last to saturate in the Fe(II) titration and is free from the contribution of the Fe(II)-aqua MCD signal (Figure 1B) and thus should only reflect the coupled binuclear ground state.[3] The VTVH MCD curves are nested, with the high-temperature data offset from the low-temperature data when the isotherms are plotted as a function of $\beta H/2kT$. This is associated with the rhombic zero-field splitting (ZFS) of a non-Kramers doublet ground state and arises from nonlinear field-induced mixing between the sublevels of the doublet (*47*).

The ground state analysis of the VTVH MCD data of a reduced non-heme binuclear active site can be accomplished using two complementary models: (1) the doublet model: for non-Kramers systems, this allows for the contribution of the second-order Zeeman affect to be included as a linear *B*-term that results from the field induced mixing between different doublets. The ground state parameters obtained are then analyzed using a spin-Hamiltonian and (2) the spin-projection model: the dimer wave functions are calculated based on the fact that the MCD intensity is proportional to the spin-expectation values of the iron center being studied by VTVH MCD projected on the dimer wave functions. Both models are applied next to analyze the ground state of mouse R2, while the spin-projection model is also applied to our past data on the ground state of *E. coli* R2 that had also been analyzed using the doublet model (*42*, *48*).

(A) Doublet Model. The VTVH MCD data were fit using the MCD intensity expression for a non-Kramers system, allowing for the effects of a linear *B*-term from field induced mixing between states and the presence of thermally excited sublevels of the ground state, eq 2 (*49*−*53*)

$$\Delta\epsilon = \sum_i \left[(A_{\mathrm{satlim}})_i \left(\int_0^{\pi/2} \frac{\cos^2\theta \sin\theta}{\Gamma_i} g_{\|i} \beta H \alpha_i \, d\theta - \sqrt{2}\frac{M_z}{M_{xy}} \int_0^{\pi/2} \frac{\sin^3\theta}{\Gamma_i} g_{\perp i} \beta H \alpha_i \, d\theta \right) + B_i H \gamma_i \right] \quad (2)$$

where

$$\Gamma_i = \sqrt{{\delta_i}^2 + (g_{\|i}\beta H \cos\theta)^2 + (g_{\perp i}\beta H \sin\theta)^2}$$

$$\alpha_i = \frac{e^{-(E_i-\Gamma_i/2)/kT} - e^{-(E_i+\Gamma_i/2)/kT}}{\sum_j e^{-(E_j-\Gamma_j/2)/kT} + e^{-(E_j+\Gamma_j/2)/kT}}$$

$$\gamma_i = \frac{e^{-(E_i-\delta_i/2)/kT} - e^{-(E_i+\delta_i/2)/kT}}{\sum_j e^{-(E_j-\delta_j/2)/kT} + e^{-(E_j+\delta_j/2)/kT}}$$

$(A_{\mathrm{satlim}})_i$, B_i, δ_i, $g_{\|i}$, and $g_{\perp i}$ are the *C*- and *B*-term MCD intensity, the rhombic ZFS, and the dimer *g* values of the *i*th doublet, respectively. E_i is the energy of the *i*th sublevel, and the energy of the ground state is defined as zero. The Boltzmann population over all states has been included in both the *C*-term and the *B*-term intensity (A_{satlim} and *B* parameters, respectively) as the factors α_i and γ_i, respectively. *H* is the applied magnetic field, *k* is the Boltzmann constant, and M_z and $M_{x,y}$ are the transition dipole moments for the directions indicated. Different combinations of these parameters lead to different VTVH MCD behaviors.

The lowest temperature (1.9 K) data collected at 6250 cm^{-1} were fit first using eq 2. The $(A_{\mathrm{satlim}})_0$, B_0, δ_0, and $g_{\|}$ are adjustable parameters, while $g_{\perp}$ and the polarization ratio $M_z/M_{x,y}$ were initially fixed at zero (but later allowed to float to improve the fit). A good fit to the reduced mouse R2 saturation data taken from 1.9−7 K requires a single non-Kramers doublet having $g_{\|} \sim 8$ and $\delta \sim 2$ cm^{-1}, indicating an $M_s = \pm 2$ ground state. The fit curve starts to deviate from the data at temperatures >7 K, indicating that the contribution from an excited sublevel becomes significant (Supporting Information, Figure S1).

An excited doublet at ~4 cm^{-1} above the ground state is required to fit the high-temperature variable-field saturation data. The fitting was performed by holding the best fit ground

[3] Note that the VTVH data taken at 10 000 cm^{-1} cannot be analyzed since the contribution of the Fe(II)-aqua complex to the MCD signal cannot be accurately removed from the VTVH data.

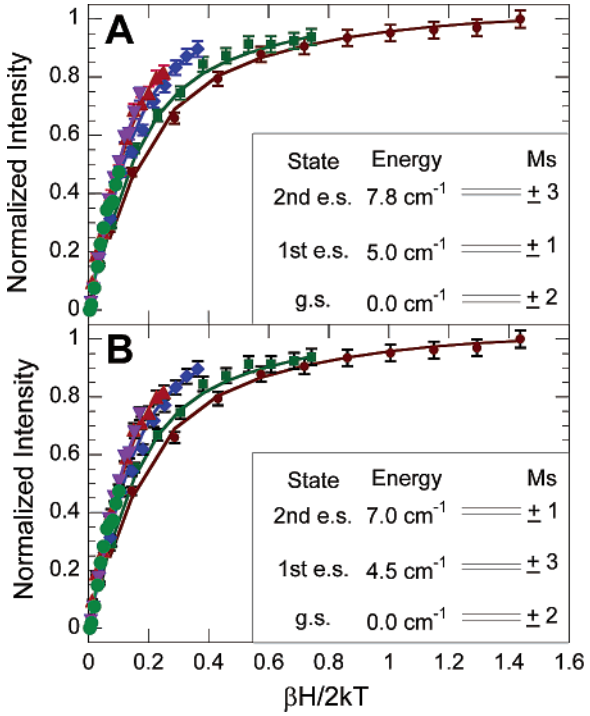

FIGURE 4: Saturation magnetization behavior of the MCD signal for reduced mouse RNR R2 at 6250 cm^{-1}. The intensity amplitude (symbols) for a range of magnetic fields (0−7.0 T) at a series of fixed temperatures is plotted as a function of $\beta H/2kT$. The fits to the VTVH MCD data (solid lines) were obtained using eq 2 with the parameters given in Table 1. (A) Fit with $M_s = \pm 1$ as the first excited state. (B) Fit with $M_s = \pm 3$ as the first excited state. The resultant energy level diagrams are presented in the insets.

state parameters constant and allowing the parameters associated with an excited state, including A_{satlim} and B parameters, δ, and energy, to float. The $g_{||}$ value associated with the excited sublevel was initially fixed at 4 (i.e., $M_s = \pm 1$, a possible excited state derived from the energy level diagram obtained from a spin-Hamiltonian analysis, vide infra) but was allowed to float to improve the fit. Inclusion of this $M_s = \pm 1$ sublevel at ~5 cm^{-1} above the $M_s = \pm 2$ doublet significantly improves the fit. Even with the addition of this excited state, the fit curve starts to deviate at temperatures >15 K. This indicates that an additional excited sublevel starts to contribute. From the spin-Hamiltonian analysis in section 2B (vide infra), $M_s = \pm 3$ can be a possible second excited state. Thus, the fit was improved by adding a second excited state with $g_{||}$ ~12 at ~8 cm^{-1} (Figure 4A). This generates a ground sublevel of $M_s = \pm 2$ with two excited states of $M_s = \pm 1$ and ± 3 at ~5 and ~8 cm^{-1} above the ground state. The parameters obtained are given in Table 1A. The error range of each parameter included in Table 1 was estimated by floating the parameter with the rest of the parameters fixed until the calculated curves deviated from the data points.

In addition, the VTVH MCD data can be fit equally well by adding a first excited state with $M_s = \pm 3$ and a second excited state of $M_s = \pm 1$ at ~4.5 and ~7 cm^{-1} above the $M_s = \pm 2$ ground state (Figure 4B and Table 1B), which is an alternative solution from the spin-Hamiltonian analysis (vide infra). The error range of these excited state energies was determined by systematically evaluating the quality of fits with the excited state energies fixed and the A_{satlim} and B parameters varied. Fits were considered unacceptable either when the fitting curves missed the error bars in the data points or when the magnitude of the B parameter became larger than the A_{satlim} parameter. In summary, good fits for the VTVH MCD of reduced mouse R2 require a ground state of $M_s = \pm 2$ and two excited states with $M_s = \pm 1$ and ± 3, with the energy order of the two excited states producing indistinguishable results (Figure 4A,B).

(B) Spin-Hamiltonian Analysis. To analyze the ground state associated with the VTVH MCD data on reduced R2, we consider the electronic structure of a coupled binuclear ferrous system. A high-spin ferrous ion has an $S = 2$ ground state with $M_s = 0$, ± 1, and ± 2. This 5-fold degeneracy will split in energy due to zero-field splitting, which is defined by axial and rhombic spin-Hamiltonian parameters. In an exchange coupled system, the two ferrous ions can also interact through bridging ligands to give $S_{tot} = |S_1 + S_2| \cdot\cdot \cdot\cdot |S_1 - S_2| = 4, 3, 2, 1$, and 0 levels. These levels are split in energy by the exchange coupling $H = -2JS_1S_2$ to generate $(2S_{tot} + 1)M_s$ degenerate levels, which are further split in energy by zero-field splitting (ZFS). Since the magnitude of D and J is comparable in coupled binuclear non-heme ferrous systems, their combined effects need to be considered.

A spin-Hamiltonian analysis has been performed on the VTVH MCD results. Eq 3 gives an expression of the spin-Hamiltonian for a general non-heme biferrous system, which operates on the uncoupled basis set $|S_1, S_2, M_{s1}, M_{s2}>$, where the subscripts indicate the two ferrous centers

$$H = -2J\hat{S}\cdot\hat{S}_2 + D_1(\hat{S}_{z1}^2 - 1/3S(S+1)) + E_1(\hat{S}_{x1}^2 - \hat{S}_{y1}^2) + D_2(\hat{S}_{z2}^2 - 1/3S(S+1)) + E_2(\hat{S}_{x2}^2 - \hat{S}_{y2}^2) + g_{z1}\beta H_z\hat{S}_{z1} + g_{x1}\beta H_x\hat{S}_{x1} + g_{y1}\beta H_y\hat{S}_{y1} + g_{z2}\beta H_z\hat{S}_{z2} + g_{x2}\beta H_x\hat{S}_{x2} + g_{y2}\beta H_y\hat{S}_{y2} \quad (3)$$

J is the isotropic exchange coupling between the two iron sites; D_1, D_2, E_1, and E_2 are the axial and rhombic ZFS parameters for each iron arising from local spin−orbit coupling; and H is the magnetic field. Zeeman terms ($g_{z1}\beta H_{z1}S_{z1}$,...etc.) are also included, where the g value can be coupled to the ZFS parameters using ligand field theory as given in eq 4a,b. λ is the Fe(II) ground state spin−orbit coupling constant (~100 cm^{-1}), and k^2 is the Stevens orbital reduction factor, which is <1 due to covalency.

$$D_{Fe^{2+}} = \frac{-k^2\lambda}{4}(g_{xFe^{2+}} + g_{yFe^{2+}} - 2g_{zFe^{2+}}) \quad (4a)$$

$$E_{Fe^{2+}} = \frac{-k^2\lambda}{4}(g_{yxFe^{2+}} - g_{xFe^{2+}}) \quad (4b)$$

Application of eq 3 to the uncoupled basis generates a 25 × 25 matrix. Diagonalization of this matrix in zero magnetic field gives the wave functions of the binuclear ferrous spin states and their energies, which are dependent on the relative magnitudes of the exchange coupling and the ZFS. The magnitude of the D values are constrained to be less than |15| cm^{-1} (the largest value from model systems and ligand field calculations); the maximum $|E/D|$ is 1/3.

From the excited state CD and MCD spectroscopy, the two ferrous sites are 5-coordinate trigonal bipyramidal and 4-coordinate distorted tetrahedral, which indicates that the two sites have ZFS parameters with negative and positive

Table 1: Summary of MCD Parameters for the Ground and Excited States of Reduced Binuclear Non-Heme Mouse Ribonucleotide Reductase (Mouse R2) at 6250 cm^{-1} and *E. coli* Ribonucleotide Reductase (*E. coli* R2) at 7700 cm^{-1}

A. VTVH MCD Fit of Mouse R2 at 6250 cm^{-1} with $J < 0$

	$M_s = \pm2$	$M_s = \pm1$	$M_s = \pm3$
$g_{\|\|}$	8.00 ± 0.3	4.00 ± 0.3	12.00 ± 0.05
δ	1.96 ± 0.2	1.72 ± 0.2	2.71 ± 0.03
A	1.70 ± 0.2	6.18 ± 0.3	2.50 ± 0.05
B	1.92 ± 0.02	−5.54 ± 0.04	12.55 ± 0.02
$g_\perp$	0.13 ± 0.02	0.13 ± 0.02	0.13 ± 0.02
$M_z/Mx,y$	0.13 ± 0.02	0.13 ± 0.02	0.13 ± 0.02
energy (cm^{-1})	0.00 ± 0.0	5.01 ± 0.4	7.83 ± 0.04

B. VTVH MCD Fit of Mouse R2 at 6250 cm^{-1} with $J > 0$

	$M_s = \pm2$	$M_s = \pm3$	$M_s = \pm1$
$g_{\|\|}$	8.00 ± 0.3	12.00 ± 0.5	4.00 ± 0.03
δ	1.96 ± 0.2	1.72 ± 0.2	2.71 ± 0.03
A	1.70 ± 0.2	1.54 ± 0.1	7.16 ± 0.05
B	1.92 ± 0.02	−1.57 ± 0.04	−0.32 ± 0.02
$g_\perp$	0.13 ± 0.02	0.13 ± 0.02	0.13 ± 0.02
$M_z/Mx,y$	0.13 ± 0.02	0.13 ± 0.02	0.13 ± 0.02
energy (cm^{-1})	0.00 ± 0.0	4.50 ± 0.3	7.02 ± 0.04

C. VTVH MCD Fit of *E. coli* R2 at 7700 cm^{-1}

	$M_s = \pm2$	$M_s = \pm1$
$g_{\|\|}$	8.00 ± 0.3	4.00 ± 0.3
δ	3.52 ± 0.2	10.1 ± 0.2
A	1.23 ± 0.2	2.69 ± 0.3
B	13.9 ± 0.2	−6.2 ± 0.4
$g_\perp$	0.0 ± 0.02	0.0 ± 0.02
$M_z/Mx,y$	0.0 ± 0.02	0.0 ± 0.02
energy (cm^{-1})	0.00 ± 0.0	4.03 ± 0.4

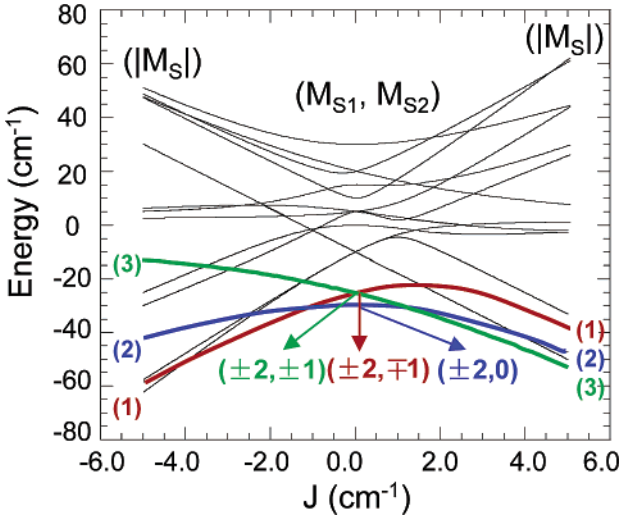

FIGURE 5: Correlation diagram of the energy levels of the binuclear ferrous ground state with opposite signed ZFS and exchange coupling. The axial ZFS parameters (D) on the two iron atoms are held constant at $D_1 = -10$ cm^{-1} and $D_2 = +5$ cm^{-1}. The exchange coupling (J) is varied from −5 to +5 cm^{-1}. Each line in the figure represents a spin state (labeled with M_S or M_{Si}), which changes in energy as J is varied. The central portion gives the pure ZFS limit with states labeled with M_{Si} values for each uncoupled Fe(II) (M_{S1}, M_{S2}). The right side indicates a ferromagnetic interaction ($J > 0$) between the ferrous ions labeled with the total M_S value for the coupled site and the left side an antiferromagnetic interaction ($J < 0$) labeled with the total M_S value. Colored lines indicate the ground and excited states discussed in the present study. The spin Hamiltonian used for calculating the levels is given in eq 3, with $E_1 = E_2 = 0$ and $H_x = H_y = H_z = 0$.

signs (*53*). Figure 5 presents the energy level diagram generated for $D_1 = -10$ cm^{-1}, $D_2 = +5$ cm^{-1}, and axial ($E_1 = E_2 = 0$) symmetry for a range of J values from −5 to +5 cm^{-1} (Note: combinations of either two positive or two negative D values do not give the experimental $M_s = \pm2$ ground state, see Figure 7B in ref *53*). The right side of Figure 5 corresponds to ferromagnetic coupling ($J > 0$). This results in an (S_{tot}, $|M_s|$) = (2,2) ground state when J is small but changes to (3,3) when $J > \sim1$ cm^{-1} (red lines), with different excited states dependent on the magnitude of J. The left side gives the antiferromagnetic coupling case ($J < 0$), which generates a different ground state as J becomes more negative: (S_{tot}, $|M_s|$) = (2,2), (1,1), or (0,0).

From the VTVH MCD analysis, a ground state of $M_s = \pm2$ is required, which limites the range of J to be $-1 < J < +1$ cm^{-1} with the first excited state being $M_s = \pm3$ when $J > 0$ and $M_s = \pm1$ when $J < 0$. Although the sign of J cannot be defined, as these two sets of excited states give equivalent VTVH MCD fits, limits in the magnitude of J can be estimated from the following results: (1) extending the spin-Hamiltonian analysis to include the presence of a magnetic field shows that the first excited state crossovers become the ground state regardless of the sign of J when $J > +0.5$ or < -0.5 cm^{-1}. This would lead to a change in the slope in the low-temperature low-field data, which is not observed in Figure 4. (2) Spin-Hamiltonian calculations with different magnitudes of the ZFS parameters show that when $-0.2 < J < +0.2$, no combination of D gives excited state energies that fall into the range of that obtained from the VTVH MCD data (Table 1A,B). Thus, the range of J is $0.2 < |J| < 0.5$. The results from the spin-Hamiltonian analysis are summarized in Table 2A. The binuclear Fe(II) active site of mouse R2 requires two weakly coupled Fe(II)s with opposite signs for their ZFS D values.

(C) Spin-Projection Model. In the previous VTVH MCD analysis, second-order Zeeman interactions between levels have been included via the experimental B-term parameter contribution to MCD intensity. A complementary fitting approach to the VTVH MCD data was also performed by using the dimer wave functions from eq 3 and the fact that the MCD intensity is proportional to the spin-expectation values of the single iron center being studied by MCD projected onto the dimer states. This is from eq 26 in ref *54* modified to include the spin-projection on the biferrous states (*55*). Fitting parameters include D_1, E_1, D_2, E_2, J, and the effective transition moment products M_{xy}, M_{xz}, and M_{yz}.

Good fit to the VTVH MCD data for the 6250 cm^{-1} band cannot be obtained when the two ZFS D values have same sign (Figure 6A), indicating that a pair of ZFS D values with opposite signs is required. Furthermore, good fit to the MCD data could not be obtained if it is assumed that this transition is associated with Fe(II) with a negative D value (D_2) (Figure 6B). Alternatively, when this transition is associated with the Fe(II) center with the positive D (D_2), the fits are significantly improved especially for the lowest temperature curve (Figure 6C). This improvement of fit is critical since at this temperature the dimer wave function only reflects the ground state. Thus, the result indicates that the iron center associated with this MCD transition at 6250 cm^{-1} has the positive zero-field splitting, which is associated with a 4-coordinate structure for this iron center. It should be noted that both negative and positive J values generate indistin-

Table 2: Summary of Spin-Hamiltonian Parameters for (1) Reduced Binuclear Non-Heme Mouse Ribonucleotide Reductase Obtained Using (A) the Doublet Model with Spin-Hamiltonian Analysis, (B) the Spin-Projection Model, and (C) by Simulation of the Magnetic Susceptibility Data (*40*) and (2) Reduced Binuclear Non-Heme *E. coli* Ribonucleotide Reductase Obtained Using (D) the Spin-Projection Model

	1. reduced mouse R2			2. reduced *E. coli* R2
	A. doublet model	B. spin-projection model	C. SQUID simulation	D. spin-projection model
J (cm^{-1})	$0.2 < \|J\| < 0.5$	$-0.5 < J < 0.5$	0	$-0.65 < J < -0.3$
D_1 (cm^{-1})	$-15 < D_1 < -10$	$-15 < D_1 < -10$	+9	$-11 < D_1 < -7$
E_1/D_1 (cm^{-1})	>0	0.23−0.33	0.22	0.33
D_2 (cm^{-1})	$+7 < D_2 < +10$	$+8 < D_2 < +10$	+9	$+3 < D_2 < +9$
E_2/D_2 (cm^{-1})	>0	0.23−0.33	0.22	0.32
polarization	N/A	5% *z*, 50% *y*, 45% *x*	N/A	69% *z*, 16% *y*, 16% *x*

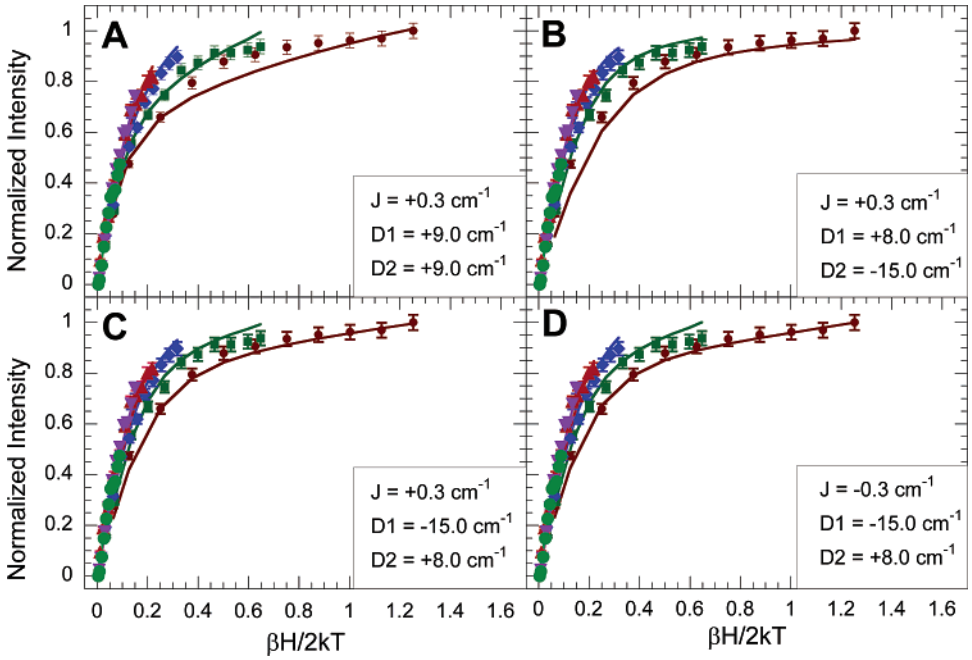

FIGURE 6: Saturation magnetization behavior of the MCD signal for reduced mouse RNR R2 at 6250 cm^{-1}. The intensity amplitude (symbols) for a range of magnetic fields (0−7.0 T) at a series of fixed temperatures is plotted as a function of $\beta H/2kT$. The fits to the VTVH MCD data (solid lines) were obtained using eq 26 in ref *54* modified based on the fact that the MCD intensity is proportional to the spin-expectation values of the single iron center being studied by MCD projected on the dimer states. The resultant fit parameters are presented in the inset. D_2 is the ZFS of the iron center associated with the 6250 cm^{-1} transition. Fit with (A) $D_1 > 0$, $D_2 > 0$, $J > 0$; (B) $D_1 > 0$, $D_2 < 0$, $J > 0$; (C) $D_1 < 0$, $D_2 > 0$, $J > 0$; and (D) $D_1 < 0$, $D_2 > 0$, $J < 0$.

guishably good fits (compare Figure 6C,D). This is consistent with the ground state analysis using the doublet model (vide supra). The best fit to the VTVH MCD data using the spin-projection model is shown in Figure 6C and is summarized in Table 2B, with $-0.5 < J < +0.5$ cm^{-1}, $-15 < D_1 < -10$ cm^{-1}, $+7 < D_2 < +10$ cm^{-1}, and both Fe(II) centers rhombic.

The spin-projection model was also applied to our past VTVH MCD data collected at 7700 cm^{-1} on *E. coli* R2 in ref *48* for comparison. It has been demonstrated from our prior results in Fe(II) binding titrations and electronic structure calculations that this transition is associated with the 4-coordinate ferrous site with a positive ZFS D value. Fitting results are included in the Supporting Information Figure S2, and the parameters are summarized in Table 2D. The data for *E. coli* R2 can only be fit using the spin-projection model with two opposite-signed ZFSs. In addition, a good fit requires that the two ferrous centers be weakly antiferromagnetically coupled ($-0.65 < J < -0.3$. Fitting the VTVH MCD data at 7700 cm^{-1} using the Fe(II) with a positive ZFS D_2 requires this transition to be polarized in the z direction.

DISCUSSION

This study utilized a combination of CD/MCD/VTVH MCD spectroscopic techniques to obtain insight into the geometric and electronic structure of the binuclear ferrous center of mouse R2. This enzyme is the first mammalian RNR R2 system studied using this methodology, which provides a basis for comparison to *E. coli* R2 and other similar Fe(II) enzymes. The CD and MCD spectra showed that three ligand field transitions are associated with the active site of reduced mouse R2. Titration of ferrous ion to the apo form and the ligand field analysis indicated that the two transitions in the low-energy region (5500 and 6700 cm^{-1}) are from a 4-coordinate iron and that the high-energy transition at 9900 cm^{-1} is from a 5-coordinate iron. The VTVH MCD analysis using the doublet model with the spin-Hamiltonian showed that reduced mouse R2 has a ground state of $M_s = \pm 2$ and two excited states with $M_s = \pm 1$ and ± 3. This result gives two irons with opposite signs of their ZFS, $-15 < D_1 < -10$ cm^{-1} and $+8 < D_2 < +10$ cm^{-1}; the two irons are weakly exchange coupled, with $0.2 < |J| < 0.5$ cm^{-1}, indicating the presence of carboxylate bridges.

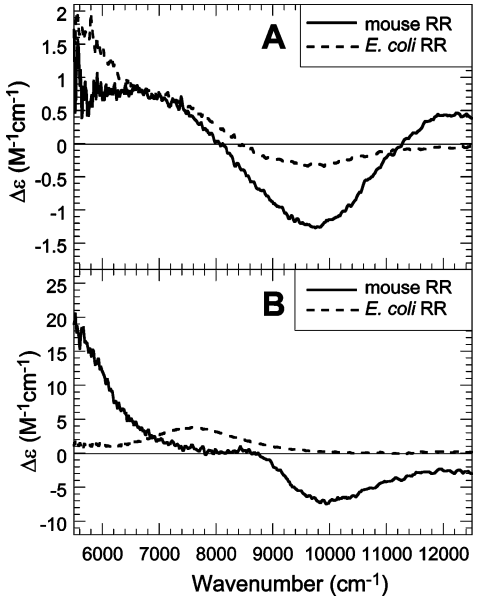

FIGURE 7: (A) CD spectra of the reduced binuclear non-heme Fe(II)Fe(II) active site of ribonucleotide reductase R2 from mouse (—) and ribonucleotide reductase R2 from *E. coli* (- - -). The CD spectra were recorded at 5 °C. (B) LT MCD spectra of the reduced binuclear non-heme Fe(II)Fe(II) active site of ribonucleotide reductase mouse R2 (—) and ribonucleotide reductase R2 *E. coli* (- - -). The low-temperature MCD spectra were recorded at 5 K and 7 T. The data for *E. coli* R2 are adapted from ref *48*.

In addition, the VTVH MCD analysis using the spin-projection model shows that the Fe(II) associated with the ligand-field transition at 5500 cm^{-1} has the positive ZFS. This further supports its assignment as a transition associated with the 4-coordinate site.

(1) Ground State Analysis: Comparison to Past Results. The ground state of mouse R2 has been studied using SQUID magnetic susceptibility (*40*), and the results are summarized in Table 2C. The magnetization data were interpreted to indicate that the two Fe(II)s have a positive ZFS of $D_1 = D_2 = 9$ cm^{-1}, $|E/D| = 0.22$, and no exchange coupling. Thus, the VTVH MCD analysis of biferrous mouse R2 provides an alternative interpretation of the ground state requiring weak exchange coupling and two ZFSs of opposite signs for the two iron sites. Alternatively, the VTVH MCD data cannot be fit using the results obtained from the SQUID results in Table 2C (Supporting Information, Figure S3). Thus, the MCD data show that mouse R2 is similar to *E. coli* R2 with two Fe(II) of opposite ZFS signs and weak exchange coupling. This is consistent with the presence of the carboxylate bridges between the two irons and the fact that two iron sites have different coordination environments from the different ligand field transition energies observed in CD/MCD. Even when two iron sites are at the rhombic limit, the relative signs of their ZFS are important in the MCD analysis. The signs of the ZFS determine the directionality of one iron's magnetic coordination system relative to the other, which determines the dimer *g* matrix relative to the polarization of the transitions. Therefore, the ground state generated from a pair of Fe(II) with ZFS of opposite signs is different from that generated by two Fe(II) with positive ZFS even at the rhombic limit.

(2) Spectroscopic Correlation to E. coli R2. (A) CD and MCD Spectroscopy. Figure 7 compares the CD and MCD spectra of reduced mouse R2 (solid lines) and *E. coli* R2 (dashed lines), and Table 3 summarizes the transition energies for both species. In reduced *E. coli* R2, the 5-coordinate iron has been correlated with the high-energy band (~9700 cm^{-1}), and the two low-energy bands (~5500, ~7000 cm^{-1}) are for the four-coordinate iron (*42*), which are very similar to those from mouse R2. However, differences in the CD/MCD spectra between mouse and *E. coli* R2 are also observed. While the three transitions from both species have the same sign in the CD spectra (Figure 7A), significant differences are observed in their MCD spectra (Figure 7B). (1) The high-energy band for *E. coli* R2 is not clearly present, while there is a negative transition for mouse R2. However, the MCD titration of ferrous ion for *E. coli* R2 has shown that there is a weak negative band at ~9200 cm^{-1} present when the iron content is low (*42*). Thus, this band in the MCD spectrum of holo-*E. coli* R2 is likely obscured by the intense positive transition at 7500 cm^{-1} and excess ferrous ion in solution when the active site is fully loaded with Fe(II). (2) The two low MCD energy transitions have reversed intensity relative to those for *E. coli* R2. VTVH MCD analysis using the dimer wave function has shown that for mouse R2 the intense transition at 5500 cm^{-1} (data were collected on the shoulder at 6250 cm^{-1}) for mouse R2 is (*x*,*y*) polarized (Table 2B), while for *E. coli* R2 the intense transition at 7500 cm^{-1} is *z* polarized (Table 2D), yet both transitions are associated with a 4-coordinate iron site (i.e., the Fe(II) with the positive ZFS). These results indicate that the two MCD transitions from the two different R2 are both associated with the 4-coorinate site, and the different intensities observed for the low-energy band in the MCD spectrum are due to their different polarizations. This difference reflects a geometric distortion between two 4-coordinate sites in the two R2, which is also reflected in the ligand field transition energy of this Fe(II) (Table 3, MCD transitions: 7500 cm^{-1} for *E. coli* R2 vs 6800 cm^{-1} for mouse R2) and quantitative differences in the ground state, as considered next.

Table 3: Summary of the Ligand-Field Transition Energies from the CD and MCD Gaussian Resolution Analysis for Reduced Binuclear Non-Heme Ribonucleotide Reductase from Mouse and from *E. coli* and Substrate-Bound (Stearoyl-ACP) Δ^9 Desaturase

	reduced mouse R2		reduced *E. coli* R2		reduced sub-Δ^9D	
band	CD (cm^{-1})	MCD (cm^{-1})	CD (cm^{-1})	MCD (cm^{-1})	CD (cm^{-1})	MCD (cm^{-1})
1	5600 (+)	5500 (+)	5500 (+)	5500 (+)	5000 (−)	5535 (+)
2	6700 (+)	6800 (+)	7000 (+)	7500 (+)[a]	7890 (−)	
3	9600 (−)	10000 (−)[1]	9700 (−)		9650 (−)	9156 (−)

[a] The shift in energy for this transition in MCD as compared to the same band in CD is likely due to a temperature effect.

(B) VTVH MCD and Nature of the Ground State. Differences in the VTVH MCD data were also observed between mouse and *E. coli* R2. (1) The VTVH MCD data for *E. coli* R2 showed a more nested behavior than that for mouse R2 (Figure 8, red vs black curves). (2) Fittings of the VTVH MCD data using the doublet model showed that a larger δ (the rhombic ZFS of the $M_s = \pm 2$ sublevels) is present for *E. coli* R2 (Table 1C vs A,B). (3) The ground state analysis showed that the 4-coordinate iron site in mouse R2 has a positive ZFS that is larger than that in *E. coli* R2 (Table 2B vs D). Mouse R2 had been considered to be different from

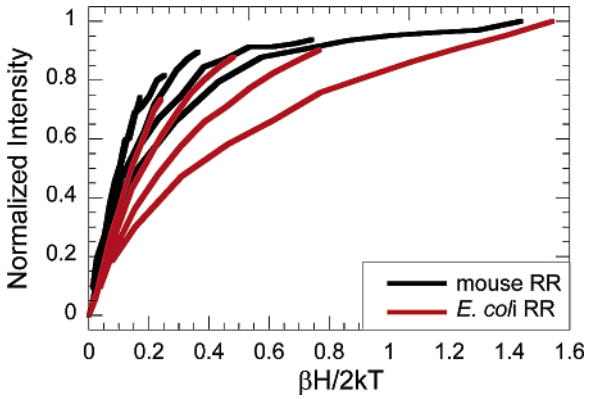

FIGURE 8: Comparison of the saturation magnetization behavior of the MCD signal in the ligand field region for reduced mouse R2 at 6250 cm^{-1} (black lines) and *E. coli* R2 at 7500 cm^{-1} (red lines). The intensity amplitude for a range of magnetic fields (0−7.0 T) at a series of fixed temperatures is plotted as a function of $\beta H/2kT$. The data for *E. coli* R2 are adapted from ref *48*.

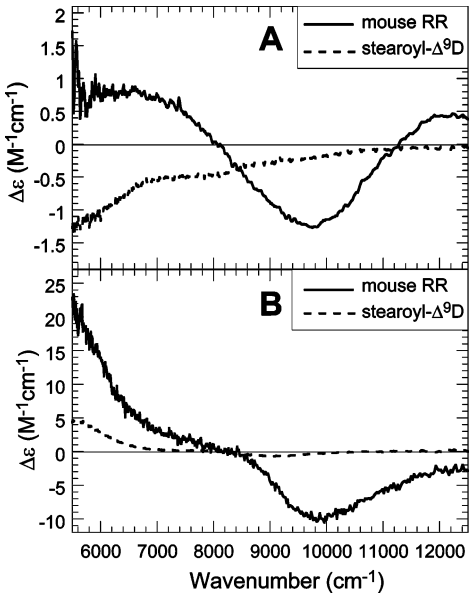

FIGURE 9: (A) CD spectra of the reduced binuclear non-heme Fe(II)Fe(II) active site of ribonucleotide reductase R2 from mouse (—) and stearoyl-ACP Δ^9 desaturase (- - -). The CD spectra were recorded at 5 °C. (B) LT MCD spectra of the reduced binuclear non-heme Fe(II)Fe(II) active site of ribonucleotide reductase R2 from mouse (—) and stearoyl-ACP Δ^9 desaturase (- - -). The low-temperature MCD spectra were recorded at 5 K and 7 T. The data for stearoyl-ACP Δ^9 desaturase are adapted from ref *55*.

E. coli R2, as the resting enzyme exhibits an integer spin EPR signal at $g_{eff} = 8$ in the presence of 20% glycerol at X-band EPR (*40*). However, our results show that there are, in fact, only small differences in the ground state that lead to a larger splitting, δ, of the $M_s = \pm 2$ for *E. coli* R2, and thus its lack of an integer spin EPR signal. This results from the decreased magnitude of the positive ZFS *D* value of the 4-coordinate Fe(II) site in *E. coli* R2, which results in a larger δ that increases the nested VTVH MCD behavior and makes the X-band integer spin EPR signal unobservable as it is too high in energy.

These results show that both mouse and *E. coli* R2 have three ligand field transitions at similar energies and that the two irons have opposite-signed ZFS and are weakly exchange coupled. The active site of mouse R2 is very similar to that of resting reduced *E. coli* R2. A small perturbation on the 4-coordinate iron site results in significant differences between the two species observed in the MCD polarization, the VTVH MCD saturation magnetization behavior, and the presence of an integer spin X-band EPR signal only in the mouse enzyme.

(3) Binding of Fe(II) to Mouse R2 as Compared to E. coli R2. In this study, a series of CD and MCD titrations was performed on apo mouse R2 with ferrous ion to determine the spectral features of each metal binding site. The two binuclear sites in the homodimer R2 subunits can, in principle, accommodate up to four irons. Analysis of the titration data shows that (1) the binding of Fe(II) is highly cooperative; (2) the two binding sites have similar low-binding affinities (*56*); (3) the Hill coefficient is 4 or higher, indicating that the two binuclear clusters are formed simultaneously; and (4) at 50% saturation the K_b is estimated to be 0.4×10^3 M^{-1}.

In contrast to mouse R2, both Mössbauer and CD/MCD data have shown that the affinity for Fe(II) for *E. coli* apoR2 is much higher and significantly different between the two sites (*48*, *57*). The 5-coordinate center binds ferrous ions at least ~5-fold more tightly than the 4-coordinate center, and at low Fe(II) concentrations this is the dominate form present (*48*). The formation of the binuclear site via binding of the 4-coordinate site does not significantly perturb the 5-coordinate site. The binding constants for the two iron centers were estimated to be $K_{b,Fe1} = \sim 14.3 \times 10^3$ M^{-1} and $K_{b,Fe2} = \sim 3.3 \times 10^3$ M^{-1}.

A greater flexibility is seen in all four carboxylate ligands of the iron cluster in mouse R2 as compared to *E. coli* R2 (*43*). This might contribute to the lower kinetic and thermodynamic affinity for Fe(II) in mouse R2 enzyme. In mouse R2, the strong cooperative formation of the two binuclear ferrous clusters could indicate a regulated process of activating the R2 protein. This is the first spectroscopic evidence for cooperative binding of iron to R2.

(4) Spectroscopic Correlation to Reduced Substrate-Bound Δ^9 Desaturase (Sub-Δ^9D). The active site of reduced Δ^9D has been described as two nearly equivalent 5-coordinated ferrous irons with a distorted square pyramidal geometry (*55*). Both irons have identical negative ZFS and are weakly antiferromagnetically coupled. Substrate-binding to reduced Δ^9D strongly perturbs the active site. The first iron remains 5-coordinate but is distorted toward a trigonal bipyramidal structure with a negative ZFS. The second iron changes to 4-coordinate with a positive ZFS. The two irons remain antiferromagnetically coupled, but the exchange coupling increases to $-J = \sim 2.5$ cm^{-1}. Thus, substrate binding to reduced Δ^9D opens an additional coordination position at one of the irons, which significantly increases the O_2 reactivity. Figure 9A,B compares the CD/MCD spectra of substrate-bound Δ^9D to those of resting reduced mouse R2, and the ligand field transitions are summarized in Table 3. Both species show three transitions at similar energies in the CD and MCD spectra. The CD transitions for mouse R2 have different signs from those for sub-Δ^9D; however, their MCD spectra look extremely similar. In addition, both species have weak exchange coupling between the two irons and opposite signs of their ZFS. Thus, substrate binding changes the biferrous active site of Δ^9D to become similar to that of resting reduced mouse R2, where Δ^9D can rapidly

react with O_2 only with substrate bound, and R2 reacts with O_2 in the resting state. These studies define a common reactive active site structure for both classes of enzymes.

In summary, this study presents detailed electronic and geometric structure insight into the [Fe(II)Fe(II)] active site in a mammalian R2 enzyme. This spectroscopic methodology shows that the biferrous center for mouse R2 consists of one 5- and one 4-coordinate iron. The ground state analysis shows that the 4-coordinate site has a positive ZFS, while the 5-cordinate site has a negative ZFS, and the two irons are weakly exchange coupled. The active site structure obtained for the reduced form of mouse R2 has been correlated to that for *E. coli* R2 and substrate-bound Δ^9D. These three species all have one 5-coordinate and one 4-coordinate iron that are weakly exchange coupled and serve as a common structural motif for the dioxygen reactive forms of R2 and Δ^9D in the presence of substrate. Previous calculations performed on the biferrous active site of *E. coli* R2 have indicated that it is difficult to reduce dioxygen to peroxide by a mechanism where O_2 binds to one Fe and the second electron is transferred from the unbound Fe through the carboxylate bridges (which provide poor superexchange pathways), as opposed to dioxygen bridging the two irons allowing concerted 2-electron transfer to form peroxide (*42*). Thus, the strong correlation of spectral features demonstrates that a common geometric and electronic structure exists for the dioxygen reactive site of RNR R2 and substrate-bound Δ^9D. It is now of importance to extend the analysis to methane monooxygenase (MMO), to investigate the component B effect on its dioxygen reactivity, and to develop the structure/function correlations from the three enzyme systems.

ACKNOWLEDGMENT

We thank Prof. Lars Thelander, University of Umeå for generously providing the *E. coli* strain overproducing mouse R2.

SUPPORTING INFORMATION AVAILABLE

The fit to the MCD saturation magnetization data of mouse R2 up to 10 K; the fit to the MCD saturation magnetization data of *E. coli* R2 using the spin-projection model; and the fit to the MCD saturation magnetization data of mouse R2 using the spin-projection model based on the ZFS parameters obtained from the SQUID simulation as presented in Table 2C. This material is available free of charge via the Internet at http://pubs.acs.org.

REFERENCES

1. Wallar, B. J., and Lipscomb, J. D. (1996) *Chem. Rev. 96*, 2625−2657.
2. Solomon, E. I., Brunold, T. C., Davis, M. I., Kemsley, J. N., Lee, S.-K., Lehnert, N., Neese, F., Skulan, A. J., Yang, Y.-S., and Zhou, J. (2000) *Chem. Rev. 100*, 235−349.
3. Holmes, M. A., and Stenkamp, R. E. (1991) *J. Mol. Biol. 220*, 723−737.
4. Andersson, K. K., and Gräslund, A. (1995) *Adv. Inorg. Chem. 43*, 353−408.
5. Rosenzweig, A. C., Frederick, C., Lippard, S. J., and Nordlund, P. (1993) *Nature 366*, 537−543.
6. Rosenzweig, A. C., Nordlund, P., Takahara, P. M., Frederick, C., and Lippard, S. J.(1995) *Chem. Biol. 2*, 409−418.
7. Nordlund, P., Sjöberg, B. M., and Eklund, H. (1990) *Nature 345*, 593−598.
8. Logan, D. T., Su, X. D., Åberg, A., Regnström, K., Hajdu, J., Eklund, H., and Nordlund, P. (1996) *Structure 4*, 1053−1064.
9. Lindqvist, Y., Huang, W., Schneider, G., and Shanklin, J. (1996) *EMBO J. 15*, 4081−4092.
10. Klabunde, T., Sträter, N., Fröhlich, R., Witzel, H., and Krebs, B. (1996) *J. Mol. Biol. 259*, 737−748.
11. DeMaré, F., Donald, M., Kurtz, J., and Nordlund, P. (1996) *Nature Struct. Biol. 3*, 539−546.
12. Ha, Y., Shi, D. S., Small, G. W., Theil, E. C., and Allewell, N. M. (1999) *J. Biol. Inorg. Chem. 4*, 243−256.
13. Bollinger, J. M., Jr., Tong, W. H., Ravi, N., Huynh, B. H., Edmondson, D. E., and Stubbe, J. (1999) *J. Am. Chem. Soc. 116*, 8024−8032.
14. Bollinger, J. M., Jr., Krebs, C., Vicol, A., Chen, S., Ley, B. A., Edmondson, D., and Huynh, B. H. (1998) *J. Am. Chem. Soc. 120*, 1094−1109.
15. Bollinger, J. M., Jr., Ravi, N., Tong, W. H., Edmondson, D. E., Huynh, B. H., and Stubbe, J. (1993) *J. Inorg. Biochem. 51*, 6.
16. Broadwater, J. A., Ai, J., Loehr, T. M., Sanders-Loehr, J., and Fox, B. G. (1998) *Biochemistry 37*, 14664−14671.
17. Lee, S.-K., and Lipscomb, J. D.(1999) *Biochemistry 38*, 4423−4432.
18. Lee, S.-K., Nesheim, J. C., and Lipscomb, J. D. (1993) *J. Biol. Chem. 268*, 21569−21577.
19. Liu, K. E., Valentine, A. M., Qui, D., Edmondson, D. E., Appelman, E. H., Spiro, T. G., and Lippard, S. J. (1997) *J. Am. Chem. Soc. 119*, 11134−11135.
20. Liu, K. E., Valentine, A. M., Wang, D. L., Huynh, B. H., Edmondson, D. E., Salifoglou, A., and Lippard, S. J. (1995) *J. Am. Chem. Soc. 117*, 10174−10185.
21. Moënne-Loccoz, P., Baldwin, J., Ley, B. A., Loehr, T. M., and Bollinger, J. M., Jr. (1998) *Biochemistry 37*, 14659−14663.
22. Ravi, N., Bollinger, J. M., Jr., Huynh, B. H., Edmondson, D. E., and Stubbe, J. (1994) *J. Am. Chem. Soc. 116*, 8007−8014.
23. Valentine, A. M., Stahl, S. S., and Lippard, S. J. (1999) *J. Am. Chem. Soc. 121*, 3876−3887.
24. Fox, B. G., Liu, Y., Dege, J. E., and Lipscomb, J. D. (1991) *J. Biol. Chem. 266*, 540−550.
25. Liu, K. E., Valentine, A. M., Wang, D. L., Huynh, B. H., Edmondson, D. E., Salifoglou, A., and Lippard, S. J. (1995) *J. Am. Chem. Soc. 117*, 10174−10185.
26. Broadwater, J. A., Ai, J. Y., Loehr, T. M., Sanders-Loehr, J., and Fox, B. G. (1998) *Biochemistry 37*, 14664−14671.
27. Thelander, L., and Reichard, P. (1979) *Annu. Rev. Biochem. 48*, 133−158.
28. Reichard, P. (1988) *Annu. Rev. Biochem. 57*, 349−374.
29. Reichard, P. (1993) *Science 260*, 1773−1777.
30. Jordan, A., and Reichard, P. (1998) *Annu. Rev. Biochem. 67*, 71−98.
31. Eklund, H., Uhlin, U., Färnegardh, M., Logan, D. T., and Nordlund, P. (2001) *Prog. Biophys. Mol. Biol. 77*, 177−268.
32. Sintchak, M. D., Arjara, G., Kellogg, B. A., Stubbe, J., and Drennan, C. L. (2002) *Nat. Struct. Biol. 9*, 293−300.
33. Rova, U., Goodtzova, K., Ingemarson, R., Behravan, G., Gräslund, A., and Thelander, L. (1995) *Biochemistry 34*, 4267−4275.
34. Ekberg, M., Potsch, S., Sandin, E., Thunnissen, M., Nordlund, P., Sahlin, M., and Sjöberg, B. M. (1998) *J. Biol. Chem. 273*, 21003−21008.
35. Andersson, K. K., Schmidt, P. P., Katterle, B., Strand, K. R., Palmer, A., Lee, S.-K., Solomon, E. I., Gräslund, A., and Barra, A.-L. (2003) *J. Biol. Inorg. Chem.* 8, 235−247.
36. Thelander, L., and Gräslund, A. (1994) *Met. Ions Biol. Syst. 30*, 109−129.
37. Kauppi, B., Nielsen, B. B., Ramaswamy, S., Kjøller-Larsen, I., Thelander, M., Thelander, L., and Eklund, H. (1996) *J. Mol. Biol. 262*, 706−720.
38. Mann, G. J., Gräslund, A., Ochiai, E., Ingemarson, R., and Thelander, L. (1991) *Biochemistry 30*, 1939−1947.
39. Nyholm, S., Thelander, L., and Gräslund, A. (1993) *Biochemistry 32*, 11569−11574.
40. Atta, M., Debaecker, N., Andersson, K. K., Latour, J.-M., Thelander, L., and Gräslund, A. (1996) *J. Biol. Inorg. Chem. 1*, 210−220.
41. Atta, M., Andersson, K. K., Ingemarson, R., Thelander, L., and Gräslund, A. (1994) *J. Am. Chem. Soc. 116*, 6429−6430.
42. Pulver, S. C., Tong, W. H., Bollinger, J. M., Jr., Stubbe, J., and Solomon, E. I. (1995) *J. Am. Chem. Soc. 117*, 12664−12678.
43. Strand, K. R., Karlsen, S., and Andersson, K. K. (2002) *J. Biol. Chem. 37*, 34229−34238.

44. Reem, R. C., and Solomon, E. I. (1987) *J. Am. Chem. Soc. 109*, 1216−1226.
45. Pulver, S. C., Froland, W. A., Lipscomb, J. D., and Solomon, E. I. (1993) *J. Am. Chem. Soc. 115*, 12409−12422.
46. Bradford, M. M. (1976) *Anal. Biochem. 72*, 248−254.
47. Thomson, A. J., and Johnson, M. K. (1980) *Biochem. J. 191*, 411.
48. Yang, Y.-S., Baldwin, J., Brenda, A. L., Bollinger, J. M., Jr., and Solomon, E. I. (2000) *J. Am. Chem. Soc. 122*, 8495−8510.
49. Stevens, P. J. (1974) *Annu. Rev. Phys. Chem. 25*, 201.
50. Schatz, P. N., Mowery, R. L., and Krausz, E. R. (1978) *Mol. Phys.* 35, 1537−1557.
51. Bennet, D. E., and Johnson, M. K. (1987) *Biochim. Biophys. Acta 911*, 71−80.
52. Zhang, Y., Gebhard, M. S., and Solomon, E. I. (1991) *J. Am. Chem. Soc. 113*, 5162−5175.
53. Solomon, E. I., Pavel, E. G., Loeb, K. E., and Campochiaro, C. (1995) *Coord. Chem. Rev. 144*, 369−460.
54. Neese, F., and Solomon, E. I. (1999) *Inorg. Chem. 38*, 1847−1865.
55. Yang, Y.-S., Broadwater, J. A., Pulver, S. C., Fox, B. G., and Solomon, E. I. (1999) *J. Am. Chem. Soc. 121*, 2770−2783.
56. Ochiai, E., Mann, G. J., Gräslund, A., and Thelander, L. (1990) *J. Biol. Chem. 265*, 15758−15761.
57. Bollinger, J. M., Jr., Chen, S., Parkin, S. E., Mangravite, L. M., Ley, B. A., Edmondson, D. E., and Huynh, B. H. (1997) *J. Am. Chem. Soc. 119*, 5976−5977.

BI035248Q